Draft version December 16, 2022
Typeset using LaTeX **twocolumn** style in AASTeX631

A Chemical and Kinematic Analysis of HE2226−1529

Abigail Colclasure[1] and Maya Redden[1]

[1] *Department of Physics and Kavli Institute for Astrophysics and Space Research, Massachusetts Institute of Technology, Cambridge, MA 02139, USA*

ABSTRACT

We present a chemical and kinematic analysis of a bright, low mass, metal-poor star, HE2226−1529. Data were obtained using the MIKE spectrograph at Magellan Observatory. Additional astrometric data was obtained from Gaia and photometric measurements from the USNO catalog. Chemical analysis was performed using the SMHR and STARFIT softwares. Kinematic analysis was done using the ORIENT software which produces a kinematic history of the star. We find that HE2226−1529 has [Fe/H] = −2.79 and which designates it as a Population II, Very metal-poor (VMP) star. We classify it as an r-I process star that exists in the inner halo. The complete chemical and kinematic analysis of HE2226−1529 suggests that the star was formed from the gas of a neutron star merger and asymmetric supernova in a classical dwarf galaxy and was then accreted into the Milky Way early in its history.

Keywords: Dwarf galaxies (416), Stellar kinematics (1608), Stellar dynamics (1596), Galaxy accretion (575)

1. INTRODUCTION

Metal-poor stars have a metallicity lower than one-tenth of the sun's metallicity, indicating an iron abundance ([Fe/H]) less than −2. They are classified as Population II stars which formed after the supernovae of the first stars of the universe which were metal-free and designated as Population III. Low-mass stars that formed in the early universe have changed little since their formation. Close examination of their spectra reveals information about the universe's chemical composition at the time of their formation (Becker et al. 2012). Past analyses of metal-poor stars have enabled the study of the first supernovae and their nucleosynthetic pathways (Umeda & Nomoto 2003). Other methods of observation of the early universe often require highly-advanced and expensive technologies that can detect objects far into the high redshift universe. Metal-poor stars in the Milky Way are the local equivalent of these objects.

HE2226−1529 has been identified as a metal-poor star by performing medium resolution spectroscopy on bright stars in the Hamburg/ESO survey (Frebel et al. 2006). This study confirms that finding and provides a possible nucleosynthesis interpretation and kinematic history. We summarize the observations made in section 2, analyze the stellar chemical abundance and provide stellar parameters in section 3, discuss the star's progenitor in section 4, and provide a kinematic analysis in section 5.

2. OBSERVATIONS AND MEASUREMENTS

This section provides a summary of how HE2226−1529 was observed and how basic measurements, namely the heliocentric radial velocity and the equivalent widths of the spectral features, were made.

2.1. *Telescope Observations*

Observations of HE2226−1529 were made on June 23, 2014 using the Magellan Inamori Kyocera Echelle (MIKE) spectrograph with slit size 0.70" x 5.00" at the Las Campanas Observatory in Chile. HE2226−1529 is located at R.A. = 22:29:17.31 and Dec = −15:13:53.55. The data have a signal-to-noise ratio per pixel of 151.3, 113.1, 154.4, and 131.1 at 5200 Å, 4800 Å, 6000 Å, and 6500 Å respectively. Several representative portions of the spectrum are shown in Figure 3.

2.2. *Radial Velocity Measurements*

The radial velocity of HE2226−1529 was determined using the cross-correlation method as described by Tonry & Davis (1979). The spectrum was compared to the spectrum of reference star HD140283, which is correctly calibrated to be at rest in the heliocentric frame. The measure of correlation for radial velocities in the range of −200 km/s to −100 km/s is shown in Figure 1. The adjusted spectrum from the cross-correlation method was plotted over the reference spectrum and

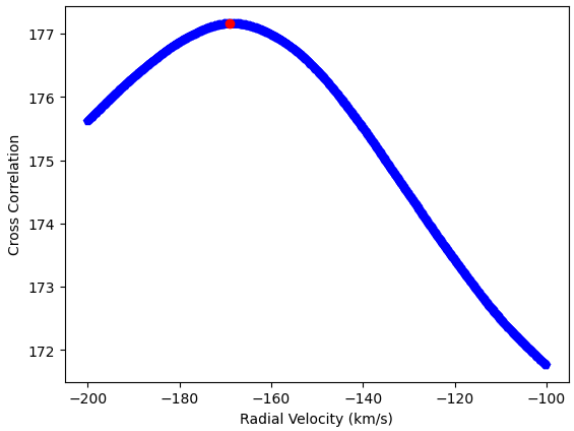

Figure 1: Cross-Correlation Result.

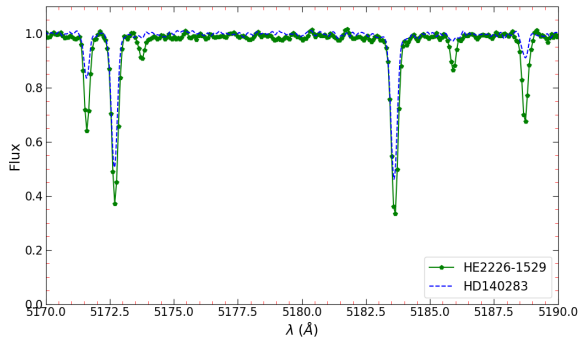

Figure 2: Radial Velocity Corrected Spectrum.

manually adjusted to minimize the difference between the corrected HE2226−1529 spectrum and the reference spectrum. The radial velocity found from this method was then corrected to be in reference to the heliocentric frame. The final heliocentric radial velocity is calculated to be −138.4 km/s and the final corrected spectrum compared to that of a standard star is shown in Figure 2.

2.3. *Summary of Spectrum*

Visual inspection of the spectrum plotted over spectra of standard stars (Figure 3) gives rough estimates for two of HE2226−1529's characteristics. The properties of the standard stars are shown in Table 1, these stars have been well studied and these data come from the literature. In the H-beta region, there is a clear relationship between temperature and the rate of dropoff around the H-beta line. We use this relationship to estimate the temperature of HE2226−1529 around 5000K. In the Mg region, the spectrum of the star is shown over the spectrum of CS22892−52 which has an effective temperature of 4800K and [Fe/H] = −3.1. Given their similar temperatures and noting that the Mg lines of HE2226−1529 are slightly stronger, the iron abundance is estimated to be around −3.0.

Standard Star	Temperature [K]	[Fe/H]
HD122563	4600	−2.7
HE1523−0901	4630	−3.0
CS22892−52	4800	−3.1
HD140283	5650	−2.5
G64−12	6450	−3.2
CD−38 245	4800	−4.1

Table 1: Standard Star Properties

2.4. *Equivalent Width Measurements*

The equivalent widths of 430 emission lines were measured using the Spectroscopy Made Harder (SMHR) software (Casey 2014). SMHR fits a curve (either Gaussian, Voigt, or Lorentzian) to each dip at known transition wavelengths. The fit of each line was checked manually and adjusted if necessary. Irregular, highly noisy, or otherwise obviously sub-standard lines were discarded during this check. The area under these curves is taken to be linearly related to the abundance of the respective element and thus the abundances are calculated. The abundances found by the equivalent width method using SMHR are shown in Tables 5-9 in the appendix and discussed further in Section 3.7.

3. CHEMICAL ABUNDANCE ANALYSIS

A chemical analysis of HE2226−1529's spectrum is used to determine the stellar parameters including metallicity, effective temperature, surface gravity, and microturbulence.

3.1. *Stellar Parameter and Abundance Determination*

The stellar parameters that were found for the star include the metallicity, effective temperature, surface gravity, and microturbulence. The parameters are calculated in an iterative process as the metallicity measured from the spectrum is dependent on the other parameters and vice versa. Initial approximations for each parameter must be made and then continuously adjusted until a stable state is reached. The final stellar parameter values are accounted for when determining chemical abundances.

A 1D model atmosphere with alpha enhancement was used for the abundance determination. Further, we required that the Fe I and Fe II abundances were in agreement with each other. We also minimized the spread of abundances of each individual Fe line across excitation potential by inspection and adjustment of all extreme outliers. This was to ensure that all measured lines would agree with a single abundance value as expected.

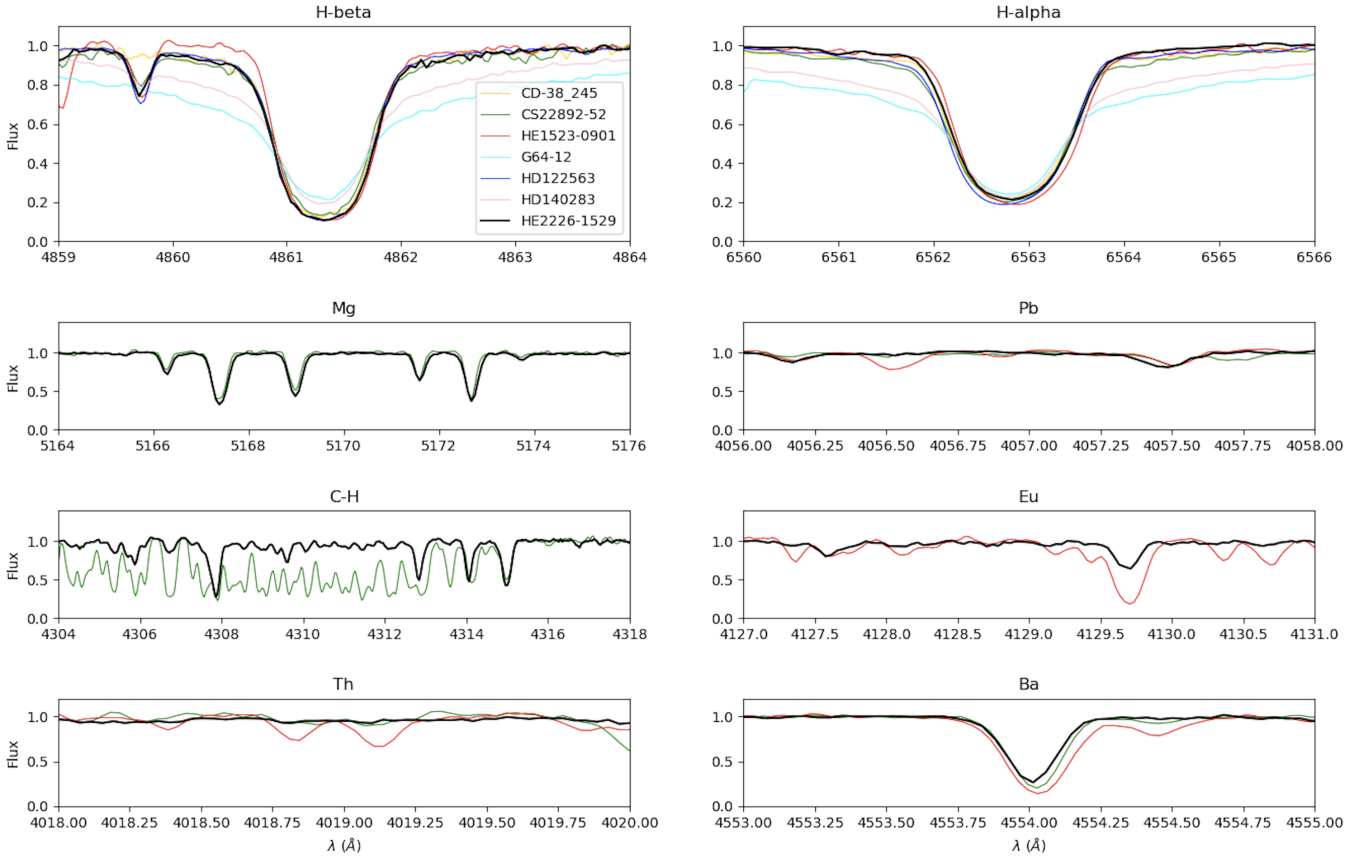

Figure 3: Spectrum Summary.

3.2. *Metallicity [Fe/H]*

Metallicity was determined from the measured equivalent widths in SMHR. [Fe/H] is measured to be −2.79 +/− 0.15. Therefore we categorize HE2226−1529 as a Population II, metal-poor star. The abundance of each measurable Fe line is shown in Figure 4. The trend is approximately flat as expected (the reader is asked to note the scale of the axes in Figure 4).

3.3. *Effective Temperature*

We calculate an effective temperature of 4915 K. The effective temperature of HE2226−1529 was determined using photometry. For these calculations, we used the photometric magnitudes given in the USNO catalog, shown in Table 2. The calculations followed the method outlined by Alonso, A. et al. (1999) and Casagrande et al. (2010).

3.4. *Surface Gravity*

The surface gravity is computed to be 1.55 +/− 0.06 dex using the parallax and fundamental equations. In order to calculate surface gravity, the bolometric correction must be computed first. It is the correction made

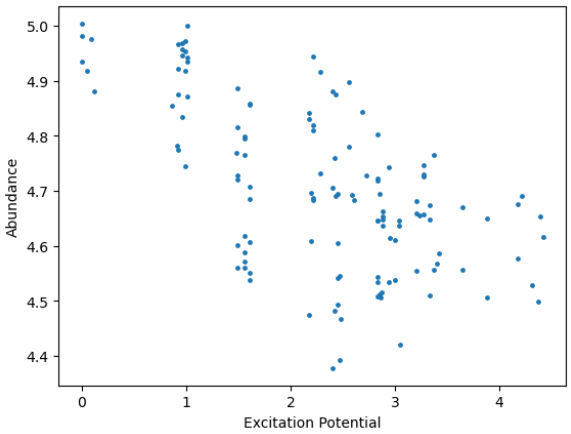

Figure 4: Abundances of Measured Iron Lines.

to the star's visible magnitude in order to obtain its absolute magnitude. Here, the bolometric correction is calculated using the method given by Alonso, A. et al. (1999) (eq. 18). We assume a stellar mass of 80 percent of the Sun's mass. This stellar mass is assumed because the star is likely to be 12-13 billion years old (due to its low metalicity) and because it is likely on the giant

Filter	Magnitude	Error
B	13	
V	12.248	0.01
g	12.656	
H	9.993	
J	10.426	0.023
K	9.923	0.025
E(B−V)	0.0341	0.0004

Table 2: Photometric Magnitudes of HE2226−1529

branch. Finally, the surface gravity is calculated using the following equation:

$$\log \frac{g}{g_\odot} = \log \frac{M}{M_\odot} + 4 \log \frac{T_{eff}}{T_{eff,\odot}} + 0.4(M_{bol} - M_{bol,\odot}) \quad (1)$$

3.5. *Microturbulence*

We compute a microturbulence of 2.15 km/s. Microturbulence is a free factor that is used to account for strong line widening caused by turbulent motion in the photosphere. It provides a correction so that the same abundance is obtained from a given element, regardless of if the line detected is weak or strong. Therefore, microturbulence has a stronger effect on stronger lines and little to no effect on weak lines. Microturbulence values can be determined by minimizing the trend in abundances versus reduced equivalent widths. A relationship between microturbulence and surface gravity has been established using data from Hansen et al. (2018), Sakari et al. (2018), Ezzeddine et al. (2020), Holmbeck et al. (2020), and Barklem et al. (2005).

3.6. *Chemical Abundance Results*

Chemical abundances can be determined using the equivalent width of each spectral line and a curve of growth. Here, this is done with SMHR. All of the observed absorption lines are sufficiently weak (unsaturated) with a small optical depth such that they fall on the linear portion of the curve of growth. Thus, the abundance can be calculated in a straightforward fashion. The spectrum synthesis method was used for determining the abundances of C-H, Sr II, Ba II, Eu II, Y, and Zr by finding the best fit synthesized spectrum to match the hyperfine structure seen in these elements' absorption patterns.

3.6.1. *Abundance Results*

Abundances for 24 elements were measured. Table 3 shows the different elements and the number of measured lines for each element N. All but 2 elements had fewer than 25 measured lines. Small sample statistics were accounted for as discussed in Section 3.9. The measured abundances of each element using the equivalent widths method is shown in Table 3. Elemental abundances of HE2226−1529 are found to be consistent with typical halo stars. In particular, this is indicated by the abundances of Cr, Mn, Co, and Ni (Hollek et al. 2011). Figure 5 provides a comparison of all measured elemental abundances to other metal-poor halo stars in the JINAbase.

Element	log ϵ(X)	[X/H]	[X/Fe]	stderr	N
C I	5.17	−3.26	−0.46	0.1	2
Na I	3.97	-2.27	0.52	0.07	2
Mg I	5.21	-2.39	0.4	0.05	5
Al I	3.14	-3.31	-0.51	0.28	2
Si I	5.34	-2.17	0.62	0.41	2
Ca I	4	-2.34	0.45	0.05	25
Sc II	0.51	-2.64	0.16	0.05	9
Ti I	2.48	-2.47	0.32	0.09	15
Ti II	2.59	-2.36	0.43	0.05	28
V II	1.38	-2.55	0.25	0.05	2
Cr I	2.63	-3.01	-0.21	0.07	10
Cr II	2.82	-2.82	-0.03	0.08	2
Mn I	2.36	-3.07	-0.27	0.1	7
Fe I	4.71	-2.79	0	0.05	129
Fe II	4.78	-2.72	0.07	0.05	13
Co I	2.24	-2.75	0.04	0.11	5
Ni I	3.52	-2.7	0.1	0.06	10
Zn I	2.18	-2.38	0.42	0.05	1
Sr II	0.45	-2.42	0.38	0.05	1
Y I	−0.6	−2.805	−0.015	0.1	1
Zr I	0.5	−2.075	0.715	0.1	1
Ba II	-0.16	-2.34	0.46	0.15	5
Eu II	-1.01	-1.53	1.26	0.2	3

Table 3: Chemical abundances of HE2226−1529.

3.6.2. *Light Element Abundance Trends*

All light element abundances fall within typical values, except for carbon. We find an unexpectedly low carbon abundance ([C/Fe]) of −0.46. This finding is peculiar because it is accompanied by a relatively high [Zn/Fe] ratio of 0.42. In a typical fallback supernova, it is expected that a high Zn abundance is accompanied by a high C abundance and a low Zn abundance is accompanied by a low C abundance. For comparison purposes, we look at the C and Zn abundances of halo stars from JINAbase with [Fe/H] greater than −3 and less than −2, as shown in Figure 6. We see HE2226−1529 as hav-

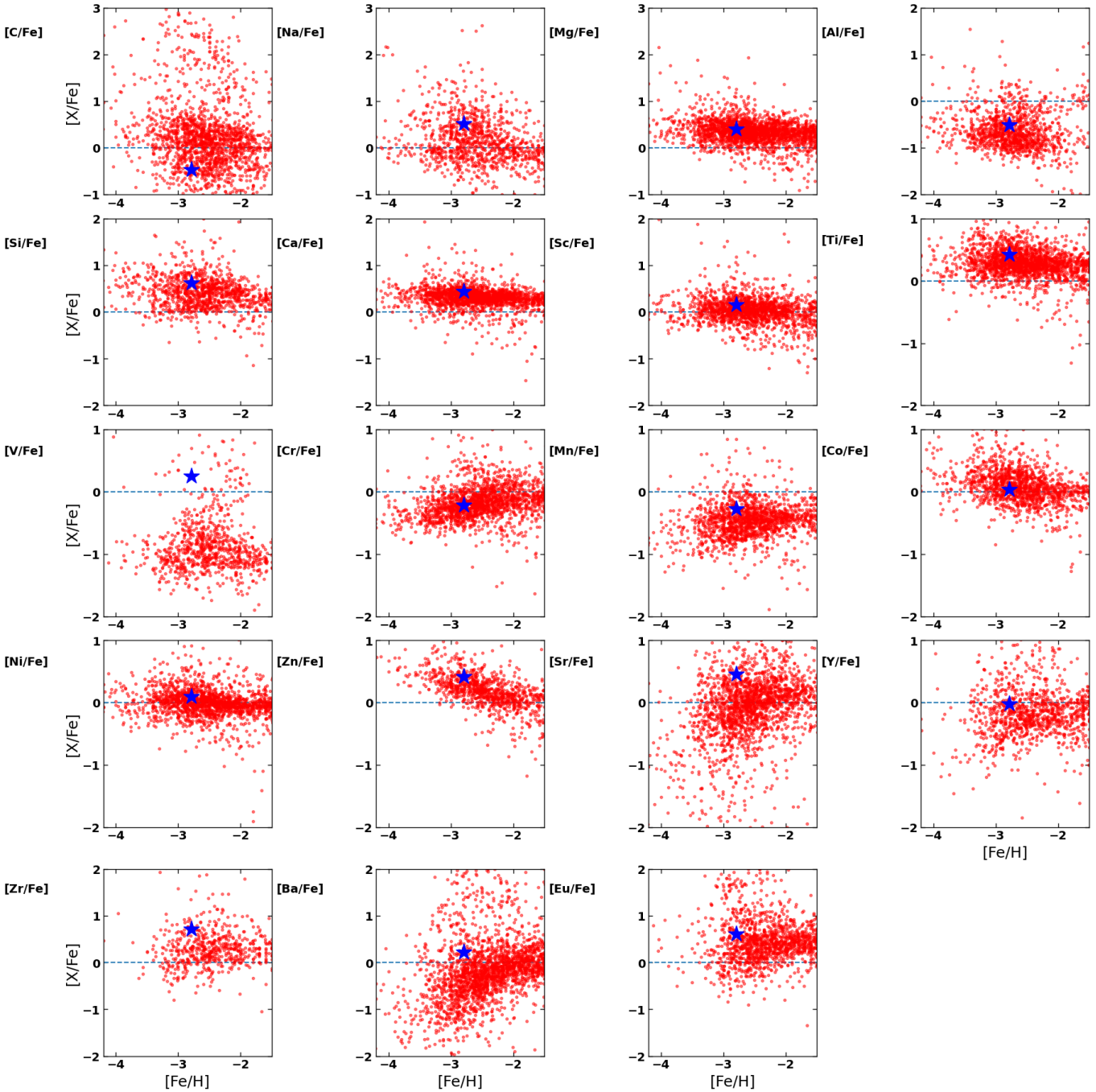

Figure 5: Abundance comparison of HE2226−1529 to other metal-poor stars from JINAbase. HE2226-1529 is identified by the blue star.

ing a lower [C/Zn] than most stars in this range. The implications of this are discussed in Section 4.

3.6.3. *Iron-peak Abundance Trends*

Like iron, the other iron-peak elements (Sc through Zn) were formed only by supernovae in the early universe. Given our low [Fe/H], we expect to see abundances for these elements that also match the predicted yield of one supernova. We see in Figure 5 that these abundances do fall among other metal-poor stars, with the exception of vanadium. This is likely due to measurement error as only 2 measurable lines were used to calculate the vanadium abundance.

3.6.4. *Heavy Element Abundance Trends*

The Eu, Ba, and Sr abundances point to an r-process star. Main r-process stars are those with [Eu/Fe] between 0.3 and 1 and [Ba/Eu] less than 0 (Beers &

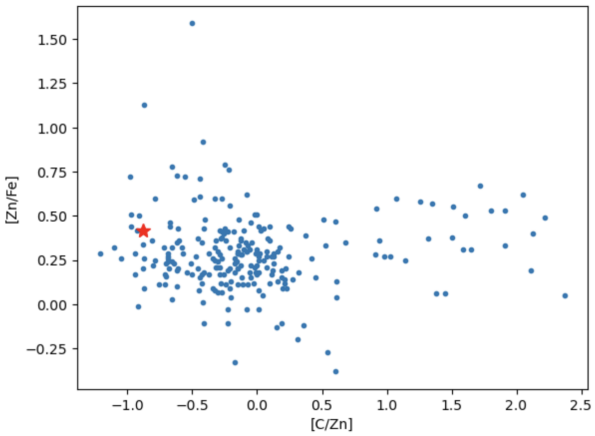

Figure 6: HE2226−1529 compared to stars in JINAbase with [Fe/H] > -3 and < -2 with respect to their C and Zn abundances. HE2226-1529 is identified by the red star.

Christlieb 2005). HE2226−1529 has [Eu/Fe] of 0.62 and [Ba/Eu] of −0.39, so it is classified as an r-I star. The implications of this classification are discussed further in Section 4.

3.7. *Abundance Uncertainties*

Random uncertainty in the abundance values arises from a number of sources including resolution limitations of the telescope and spectrograph, and choices made in the process of measuring the spectrum. Errors were given by the SMHR software based on the model fit for each absorption feature.

The standard errors of abundances measured from 25 or fewer lines were adjusted to reflect their small sample size. These adjustments were made by taking the product of the maximum difference of the abundance measurements for a given element and a factor corresponding to the number of lines as computed by small sample statistics. In addition, a minimum nominal uncertainty of 0.05 dex was applied to all elements. This minimum nominal uncertainty was determined using the Fe I lines.

We get systematic uncertainties of each abundance by varying the stellar parameters singly by their approximated statistical uncertainties and noting the change in abundance of each element. For all elements, the systematic uncertainty was found to be within three standard deviations of the error bars. This can be seen in Table 4.

Element	Random Error	$\Delta T_{\rm eff}$ +100 K	Δ logg +0.3 dex	$\Delta v_{\rm micr}$ +0.3 km s^{-1}
Na I	0.07	0.12	−0.07	−0.17
Mg I	0.05	0.09	−0.06	−0.06
Al I	0.28	0.12	−0.05	−0.17
Si I	0.41	0.12	−0.05	−0.11
Ca I	0.05	0.07	−0.02	−0.03
Sc II	0.05	0.06	0.1	−0.06
Ti I	0.09	0.13	−0.02	−0.02
Ti II	0.05	0.04	0.09	−0.08
V II	0.05	0.04	0.11	−0.01
Cr I	0.07	0.13	−0.02	−0.04
Cr II	0.08	−0.01	0.1	−0.01
Mn I	0.1	0.12	−0.02	−0.09
Fe I	0.05	0.11	−0.03	−0.07
Fe II	0.05	0.01	0.1	−0.04
Co I	0.11	0.14	−0.02	−0.09
Ni I	0.06	0.1	−0.01	−0.03
Zn I	0.05	0.06	0.05	−0.01
Sr II	0.05	0.1	0.03	−0.15
Ba II	0.15	0.09	0.08	−0.15
Eu II	0.2	0.07	0.09	−0.08

Table 4: Chemical Abundance Uncertainties

4. NUCLEOSYNTHETIC INTERPRETATION OF STELLAR ABUNDANCES

The observed abundances of HE2226−1529 can be compared to model nucleosynthesis yields from the first massive supernovae. This is done using the STARFIT tool from Monash University (Heger & Woosley 2010). STARFIT produces a model of supernova nucleosynthesis yields that most closely fits the stellar abundances. From this model and the true abundances, we gain insight into the enrichment history of the star's original nebula. This information includes the supernova explosion energy and the progenitor's mass.

We see in Figure 7 the observed element abundances do not closely fit the model produced by STARFIT. Most noticeably, we see a lower carbon abundance and a higher zinc abundance than would be predicted by the model. The most likely causes for these two differences are contradictory. The low carbon abundance suggests a low explosion energy of the gas-forming supernova and the high zinc abundance suggests a high explosion energy. We conclude that the progenitor event was not a typical fallback supernova. Possible explanations for the observed carbon and zinc abundances include an asymmetric supernova wherein the carbon was expelled at a higher velocity along a certain direction as opposed to evenly in all directions. Further analysis of this carbon and zinc signature is outside the scope of this paper.

As discussed in Section 3.6.4, europium and barium abundances of HE2226−1529 are indicative of an r-I star. The only currently accepted events wherein

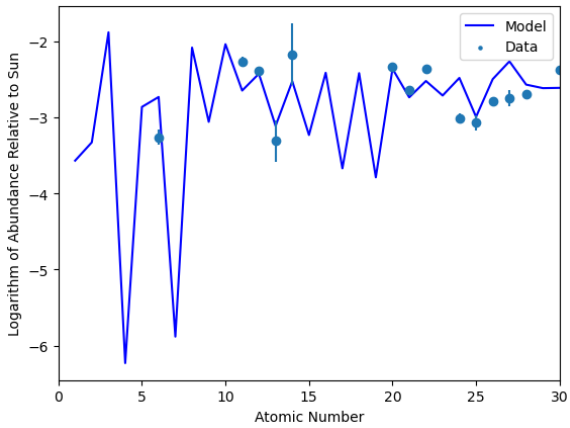

Figure 7: HE226−1529 abundances plotted over STARFIT model predictions.

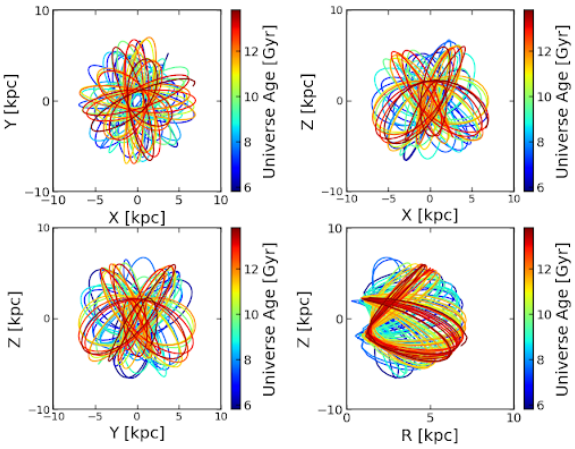

Figure 8: Orbital history of HE2226−1529 produced by the ORIENT.

r-process nucleosynthesis can occur are neutron star merger (NSM) events, therefore we assume an NSM must have occurred to produce the r-process elements in the progenitor galaxy (Ji et al. (2016), Abbott et al. (2017a), and Abbott et al. (2017b)). This suggests an upper limit on the star's age as the NSM requires adequate time to take place.

5. KINEMATIC ANALYSIS

A kinematic analysis provides important information, in addition to a chemical analysis, about a star's origin. Here, we use astrometric data obtained from Gaia DR3, as well as radial velocity measurements. These data were obtained from the Gaia mission archive website. The distance from the Earth to HE2226−1529 was calculated using its parallax. Parallax is the apparent change in the position of the star due to the Earth's orbital motion. HE2226−1529 has a parallax of 0.2163" with an error of 0.0139". The distance of the star to the Earth can be simply obtained by inverting the parallax. We compute an uncorrected distance to HE2226−1529 of 4.6 kpc. Further, a pseudocolor is not available for this star so we used a fixed zero parallax correction instead. This calculation was done following the method outlined in Lindegren et al. (2021). HE2226−1529 has a corrected distance of 3.8 kpc. Unfortunately, reliable distances from Gaia cannot be computed so simply. Small uncertainties in parallax that result from the operations of the Gaia spacecraft itself can cause large uncertainties in distance calculated. Therefore, we do a probabilistic analysis following the work of Bailer-Jones et al. (2021). A probabilistic distance is calculated using a Monte Carlo simulation that assumes an exponentially decreasing space density prior. We conclude that HE2226−1529 is located 3.8 +/− 0.2 kpc away from Earth. Thus, this star is likely located in the halo.

5.1. *Orbital Motions*

The orbital history of HE2226−1529 can be described using the ORIENT (Mardini et al. 2020), an evolution model of the Milky Way. The model uses a cosmologically derived time-varying galactic potential and back integrates to create a simulation of the orbital history of the star given its current position and velocity in the galaxy. The potential is derived from a gas and dark matter sphere and stellar matter disk.

We compute a U velocity of −44.82 km/s, a V velocity of −174.02 km/s and a W velocity of 69.25 km/s. From the simulation, we see a clear picture of HE2226−1529 moving in the inner halo as seen in Figure 8. The large negative V velocity and small maximum Z height are indicators of this. This agrees with the chemical analysis which also placed the star in the halo with high probability.

The reader should note that the orbital history created by the ORIENT model does not produce estimates of accretion times and it is possible the star was accreted after the earliest time in the simulation, approximately 8 Gyr ago. To explain its existence in the inner halo, however, it is likely HE2226−1529 was accreted early in the history of the Milky Way. After being accreted, the star would have moved in the outer halo before being pulled into the inner halo where it exists today.

6. SUMMARY AND CONCLUSIONS

Here, we presented a chemical and kinematic analysis of a bright, low mass, metal-poor star, HE2226−1529. We gave a summary of observations made and the ways in which abundances and stellar parameters were determined. We compared the chemical abundances of HE2226−1529 to other low-mass stars and fit a model to our data. We conclude that HE2226−1529 is an r-

I process star, accreted into the inner halo, and formed from an asymmetric supernova. In the future, a more in-depth kinematic analysis of may be useful to date when HE2226−1529 was accreted by the Milky Way. We also propose to repeat the analysis with a 3D model atmosphere, instead of a 1D model atmosphere.

REFERENCES

Abbott, B. P., Abbott, R., Abbott, T. D., et al. 2017a, ApJL, 848, L12, doi: 10.3847/2041-8213/aa91c9

—. 2017b, PhRvL, 119, 161101, doi: 10.1103/PhysRevLett.119.161101

Alonso, A., Arribas, S., & Martínez-Roger, C. 1999, Astron. Astrophys. Suppl. Ser., 140, 261, doi: 10.1051/aas:1999521

Bailer-Jones, C. A. L., Rybizki, J., Fouesneau, M., Demleitner, M., & Andrae, R. 2021, The Astronomical Journal, 161, 147, doi: 10.3847/1538-3881/abd806

Barklem, P. S., Christlieb, N., Beers, T. C., et al. 2005, A&A, 439, 129, doi: 10.1051/0004-6361:20052967

Becker, G. D., Sargent, W. L. W., Rauch, M., & Carswell, R. F. 2012, ApJ, 744, 91, doi: 10.1088/0004-637X/744/2/91

Beers, T. C., & Christlieb, N. 2005, ARA&A, 43, 531, doi: 10.1146/annurev.astro.42.053102.134057

Casagrande, L., Ramírez, I., Meléndez, J., Bessell, M., & Asplund, M. 2010, A&A, 512, A54, doi: 10.1051/0004-6361/200913204

Casey, A. R. 2014

Ezzeddine, R., Rasmussen, K., Frebel, A., et al. 2020, ApJ, 898, 150, doi: 10.3847/1538-4357/ab9d1a

Frebel, A., Christlieb, N., Norris, J. E., et al. 2006, ApJ, 652, 1585, doi: 10.1086/508506

Hansen, T. T., Holmbeck, E. M., Beers, T. C., et al. 2018, ApJ, 858, 92, doi: 10.3847/1538-4357/aabacc

Heger, A., & Woosley, S. E. 2010, ApJ, 724, 341, doi: 10.1088/0004-637X/724/1/341

Hollek, J. K., Frebel, A., Roederer, I. U., et al. 2011, The Astrophysical Journal, 742, 54, doi: 10.1088/0004-637X/742/1/54

Holmbeck, E. M., Hansen, T. T., Beers, T. C., et al. 2020, ApJS, 249, 30, doi: 10.3847/1538-4365/ab9c19

Ji, A. P., Frebel, A., Chiti, A., & Simon, J. D. 2016, Nature, 531, 610, doi: 10.1038/nature17425

Lindegren, L., Bastian, U., Biermann, M., et al. 2021, Astronomy &amp Astrophysics, 649, A4, doi: 10.1051/0004-6361/202039653

Mardini, M. K., Placco, V. M., Meiron, Y., et al. 2020, ApJ, 903, 88, doi: 10.3847/1538-4357/abbc13

Sakari, C. M., Placco, V. M., Farrell, E. M., et al. 2018, ApJ, 868, 110, doi: 10.3847/1538-4357/aae9df

Tonry, J., & Davis, M. 1979, AJ, 84, 1511, doi: 10.1086/112569

Umeda, H., & Nomoto, K. 2003, Nature, 422, 871, doi: 10.1038/nature01571

APPENDIX

Species	Excitation Potential	log gf	EW	abundance
Na I	0	0.11	180.15	4.024
Na I	0	−0.19	153.51	3.912
Mg I	4.35	−0.9	33.03	5.197
Mg I	4.35	−0.74	43.16	5.206
Mg I	4.33	−0.44	63.4	5.151
Mg I	2.71	−0.36	193.76	5.22
Mg I	2.72	−0.17	218.81	5.272
Al I	0	−0.64	127.48	3.363
Al I	0.01	−0.33	121.09	2.923
Si I	1.91	−1.04	175.98	5.008
Si I	1.91	−3.34	85.18	5.663
Ca I	0	0.24	186.82	3.606
Ca I	1.89	−0.2	47.09	3.766
Ca I	1.9	−0.21	46.74	3.775
Ca I	1.88	−0.41	40.63	3.844
Ca I	1.89	−0.06	103.95	4.619
Ca I	1.89	−0.55	57.32	4.266
Ca I	1.9	0.26	78.76	3.824
Ca I	1.9	−0.55	33.8	3.885
Ca I	2.52	−0.67	7.66	3.914
Ca I	2.52	−0.6	11.99	4.031
Ca I	2.52	−0.58	10.52	3.935
Ca I	2.52	0.3	43.87	3.855
Ca I	2.52	−0.6	9.62	3.912
Ca I	2.53	−0.57	13.45	4.055
Ca I	2.93	0.17	19.35	3.94
Ca I	1.88	−0.81	29.4	3.959
Ca I	1.89	−0.33	50.63	3.851
Ca I	1.9	−0.11	73.04	3.983
Ca I	2.52	−0.87	8.5	4.105
Ca I	2.53	−0.6	16.28	4.162
Ca I	2.52	0.33	55.86	3.984
Ca I	2.52	−0.55	13.34	3.991
Ca I	2.53	−0.71	14.37	4.198
Ca I	2.52	−0.81	18.78	4.424
Ca I	2.71	−0.58	9.72	4.073
Sc II	0.32	0.24	125.92	0.505
Sc II	0.59	−0.44	82.4	0.538
Sc II	0.62	−0.42	78.14	0.474
Sc II	0.6	−0.54	67.82	0.392
Sc II	0.59	−0.67	65.65	0.474
Sc II	1.36	−0.58	24.24	0.559
Sc II	1.36	−0.4	32.54	0.518
Sc II	1.77	0.02	31.96	0.531
Sc II	1.51	−0.6	22.25	0.637
Ti I	0.02	−0.13	55.23	2.296
Ti I	0.05	0.02	48.17	2.067
Ti I	0.83	−0.25	14.99	2.486
Ti I	0.84	0.35	37.35	2.405
Ti I	0.85	−0.4	42.02	3.244
Ti I	0	−1.28	8.62	2.282
Ti I	0.05	−1.01	20.61	2.498
Ti I	0.9	−0.43	10.4	2.545
Ti I	0.84	0.57	51.56	2.381
Ti I	0.84	0.45	50.84	2.489
Ti I	0.83	0.32	43.86	2.494

Table 5: Equivalent Width Measurements (1 of 5)

Species	Excitation Potential	log gf	EW	abundance
Ti I	0.05	−0.94	26.07	2.527
Ti I	0	−1.06	17.4	2.365
Ti I	0.02	−0.95	29.87	2.57
Ti I	0.05	−0.82	34.31	2.556
Ti II	1.89	−0.92	48.53	2.392
Ti II	1.08	−0.96	107.69	2.555
Ti II	1.22	−1.77	59.14	2.597
Ti II	1.08	−0.54	128.54	2.592
Ti II	1.24	−1.93	45.62	2.567
Ti II	1.24	−1.2	86.54	2.522
Ti II	1.23	−2.53	31.19	2.906
Ti II	1.17	−1.19	91.76	2.526
Ti II	1.24	−1.99	40.04	2.534
Ti II	1.08	−0.71	118.43	2.505
Ti II	1.12	−2.2	42.14	2.638
Ti II	1.08	−1.52	81.87	2.557
Ti II	1.16	−1.81	62.51	2.61
Ti II	1.17	−2.02	39.89	2.476
Ti II	1.08	−2.78	17.17	2.648
Ti II	1.12	−0.77	116.84	2.567
Ti II	1.24	−0.53	123.75	2.619
Ti II	1.57	−0.31	111.22	2.495
Ti II	1.16	−3.02	6.14	2.477
Ti II	1.24	−2.29	35.07	2.727
Ti II	1.24	−2.35	27.48	2.639
Ti II	1.08	−2.66	24.36	2.687
Ti II	1.89	−1.34	40.39	2.583
Ti II	1.89	−1.41	33.02	2.522
Ti II	1.58	−1.05	88.82	2.694
Ti II	1.58	−1.6	46.8	2.57
Ti II	1.57	−1.97	30.62	2.654
Ti II	1.58	−2.13	19.81	2.585
V II	1.82	−0.45	29.39	1.403
V II	1.8	−0.61	21.53	1.362
Cr I	0	−0.22	101.42	2.41
Cr I	0	−0.37	88.24	2.262
Cr I	1.03	−0.74	26.25	2.679
Cr I	0.98	−1.46	6.86	2.67
Cr I	0.94	0.02	70.74	2.521
Cr I	0.98	−1.36	15.08	2.906
Cr I	0.98	−1.14	19.04	2.804
Cr I	1	−0.95	23.39	2.744
Cr I	1	−1.21	12.02	2.663
Cr I	1.03	−0.67	32.92	2.69
Cr II	4.07	−0.43	16.14	2.754
Cr II	4.07	−0.65	13.53	2.883
Mn I	0	−0.5	116.71	2.454
Mn I	0	−0.65	104.44	2.283
Mn I	0	−0.84	95.1	2.245
Mn I	2.11	0.28	20.35	2.094
Mn I	2.28	−0.08	11.8	2.316
Mn I	2.89	0.3	17.08	2.811
Mn I	2.32	0.14	17.98	2.347
Fe I	1.56	−0.58	116.77	4.533
Fe I	1.49	0.28	179.67	4.717
Fe I	1.56	0.06	151.99	4.618
Fe I	1.61	−0.01	141.08	4.539
Fe I	2.83	−1.3	24.8	4.803
Fe I	1.61	−0.68	119.61	4.708
Fe I	2.83	−0.65	45.42	4.544
Fe I	1.56	−0.51	124.43	4.589
Fe I	1.49	−2.07	63.04	4.721
Fe I	2.83	−0.81	42.37	4.647
Fe I	0.91	−2.94	54.84	4.783
Fe I	2.85	−0.83	42.8	4.695
Fe I	2.83	−0.37	61.66	4.534
Fe I	2.83	−0.87	38.98	4.646

Table 6: Equivalent Width Measurements (2 of 5)

Species	Excitation Potential	log gf	EW	abundance
Fe I	2.45	−0.56	73.5	4.494
Fe I	2.42	−0.51	77.39	4.482
Fe I	2.47	−0.67	69.13	4.545
Fe I	3.33	−0.49	29.41	4.648
Fe I	3.05	0.16	71.09	4.421
Fe I	1.49	−0.69	119.67	4.561
Fe I	0	−3.36	99.31	5.004
Fe I	2.45	−0.91	60.14	4.605
Fe I	3.33	0.27	64.7	4.51
Fe I	2.48	−0.6	68.34	4.467
Fe I	3.4	−0.23	34.76	4.567
Fe I	2.47	−0.38	77.02	4.392
Fe I	1.56	−0.71	116.58	4.571
Fe I	2.4	0.08	102.23	4.378
Fe I	2.45	−0.34	87.84	4.542
Fe I	1.49	−0.17	146.8	4.601
Fe I	2.18	−0.78	77.34	4.475
Fe I	1.61	0.01	150.1	4.607
Fe I	2.22	−1.29	58.63	4.684
Fe I	0	−3	113.52	4.934
Fe I	1.56	−0.15	144.43	4.561
Fe I	1.61	−0.62	119.72	4.552
Fe I	0.05	−2.92	114.83	4.919
Fe I	2.22	−1.73	40.16	4.81
Fe I	2.2	−1.23	60.01	4.609
Fe I	2.22	−1.36	55.35	4.687
Fe I	0.09	−3.19	103.89	4.975
Fe I	2.83	−0.6	61.01	4.719
Fe I	0.12	−3.9	61.13	4.88
Fe I	2.2	−1.14	71.02	4.697
Fe I	1.48	−2.1	67.62	4.769
Fe I	1.56	−2.46	41.93	4.796
Fe I	1.49	−2.21	63.68	4.816
Fe I	2.95	−1.35	13.07	4.615
Fe I	3.27	−1.08	13.76	4.73
Fe I	1.49	−2.99	23.66	4.887
Fe I	3.21	−0.67	29.65	4.659
Fe I	2.87	−0.34	64.14	4.516
Fe I	2.88	−0.57	56.63	4.637
Fe I	2.88	−0.38	69.17	4.648
Fe I	2.85	−0.11	78.85	4.512
Fe I	2.88	−0.89	38.65	4.662
Fe I	2.86	−0.34	64.49	4.506
Fe I	2.83	0.07	89.82	4.508
Fe I	2.88	−1.08	28.24	4.653
Fe I	0.86	−3.25	48.89	4.855
Fe I	3.37	−1.11	11.42	4.766
Fe I	3.33	−0.79	19.75	4.675
Fe I	0.92	−2.97	57.46	4.774
Fe I	3.88	−0.01	19.57	4.507
Fe I	3.88	−0.12	20.79	4.65
Fe I	2.83	−0.62	63.07	4.723
Fe I	2.28	−1.36	57.19	4.732
Fe I	0.92	−2.76	82.11	4.966
Fe I	2.94	−1.04	31.75	4.743
Fe I	0.99	−3.24	48.13	4.973
Fe I	0.96	−2.84	67.22	4.834
Fe I	1.01	−3.06	60.15	5
Fe I	0.92	−3.25	46.67	4.875
Fe I	4.18	0.36	28.41	4.676
Fe I	0.99	−3.04	46.66	4.745
Fe I	1.01	−3.32	39.6	4.935
Fe I	0	−4.12	67.56	4.982
Fe I	1.49	−1.72	90.1	4.729
Fe I	3.04	−0.55	47.68	4.636

Table 7: Equivalent Width Measurements (3 of 5)

Species	Excitation Potential	log gf	EW	abundance
Fe I	3	−0.42	57.12	4.611
Fe I	1.56	−2.02	72.69	4.799
Fe I	2.22	−2.09	30.84	4.945
Fe I	2.18	−1.87	40.02	4.842
Fe I	3.27	−0.86	23.05	4.747
Fe I	1.61	−2.08	58.38	4.685
Fe I	3.21	−1.07	15.53	4.682
Fe I	2.94	−0.06	78.82	4.535
Fe I	3.27	−0.87	21.93	4.727
Fe I	3	−0.38	55.28	4.538
Fe I	3.04	−0.83	32.38	4.647
Fe I	3.24	−0.45	41.27	4.655
Fe I	1.61	−2.91	21.7	4.858
Fe I	3.21	−0.11	58.48	4.555
Fe I	1.56	−2.78	25.97	4.766
Fe I	3.27	−0.63	29.78	4.658
Fe I	1.61	−1.95	77.66	4.857
Fe I	4.42	0.44	18.55	4.617
Fe I	4.37	0.54	19.9	4.499
Fe I	0.96	−1.64	135.83	4.947
Fe I	4.31	0.64	28.26	4.529
Fe I	0.92	−1.98	121.36	4.921
Fe I	0.99	−1.85	123.37	4.919
Fe I	4.39	0.64	30.07	4.654
Fe I	0.96	−1.88	125.64	4.957
Fe I	1.01	−2.13	110.27	4.943
Fe I	1.01	−2.82	69.51	4.872
Fe I	0.96	−3.05	64.66	4.969
Fe I	0.99	−2.79	77.67	4.954
Fe I	3.42	−0.52	24.17	4.586
Fe I	3.37	−0.11	47.87	4.556
Fe I	2.56	−2.14	12.95	4.897
Fe I	2.61	−1.41	31.75	4.683
Fe I	2.45	−1.41	43.03	4.694
Fe I	2.59	−1.35	37.02	4.692
Fe I	2.43	−1.42	44.05	4.691
Fe I	2.22	−2.48	12.99	4.819
Fe I	2.56	−1.28	49.01	4.781
Fe I	2.4	−1.77	36.67	4.881
Fe I	3.65	−0.71	9.96	4.556
Fe I	2.43	−1.58	46.09	4.876
Fe I	3.65	−0.59	16.19	4.67
Fe I	2.28	−2.01	33.5	4.917
Fe I	2.18	−1.95	38.74	4.831
Fe I	2.4	−1.24	59.96	4.706
Fe I	2.73	−1.47	25.44	4.728
Fe I	2.69	−1.42	36.6	4.844
Fe I	2.42	−2.58	5.98	4.759
Fe I	4.22	−0.1	13.43	4.69
Fe I	4.18	0.12	18.2	4.578
Fe II	2.58	−2.51	50.56	4.701
Fe II	2.58	−2.02	77.5	4.67
Fe II	2.78	−2.64	37.45	4.817
Fe II	2.78	−2.57	36.21	4.722
Fe II	2.86	−2.71	28.02	4.79
Fe II	2.86	−2.42	45.14	4.812
Fe II	2.84	−2.6	35.34	4.798
Fe II	2.83	−2.4	45.55	4.762
Fe II	2.84	−2.95	20.26	4.821
Fe II	2.81	−1.94	77.56	4.806
Fe II	3.23	−2.22	33.18	4.778
Fe II	3.22	−2.18	40.32	4.857
Fe II	3.2	−2.01	47.11	4.77
Co I	0.92	−0.74	39.25	2.229

Table 8: Equivalent Width Measurements (4 of 5)

Species	Excitation Potential	log gf	EW	abundance
Co I	0.92	0.06	69.67	1.963
Co I	1.05	0.12	91.08	2.509
Co I	0.92	−0.18	67.35	2.132
Co I	0.92	−0.33	72.05	2.347
Ni I	0.42	−1.23	99.96	3.239
Ni I	3.42	−0.09	8.59	3.376
Ni I	3.38	0.25	21.84	3.453
Ni I	3.54	−0.17	8.93	3.596
Ni I	3.6	0.07	19.68	3.811
Ni I	3.65	0.32	10.65	3.305
Ni I	3.68	0.03	10.09	3.602
Ni I	1.83	−0.78	62.52	3.388
Ni I	1.68	−2.22	13.11	3.616
Ni I	1.83	−2.14	16.85	3.829
Zn I	4.08	−0.15	21.19	2.184
Sr II	0	0.15	190.37	0.451
Ba II	0	0.14	155.83	0.077
Ba II	0	−0.16	157.62	0.286
Ba II	0.6	−0.91	40.94	−0.502
Ba II	0.7	−0.03	97.29	−0.376
Ba II	0.6	−0.41	91.11	−0.263
Eu II	0	0.22	64.49	−1.168
Eu II	0	0.21	61.82	−1.225
Eu II	0.21	−0.11	64.24	−0.652

Table 9: Equivalent Width Measurements (5 of 5)